Effects of Solidification Defects on Nanoscale Mechanical Properties of Rapid Directionally Solidified Al-Cu Alloy: A Large Scale Molecular Dynamics Study

Avik Mahata[1] and Mohsen Asle Zaeem[1,2*]

[1] Department of Materials Science and Engineering, Missouri University of Science and Technology, Rolla, MO 65409, USA
[2] Department of Mechanical Engineering, Colorado School of Mines, Golden, CO 40801, USA

Abstract

Directional solidification of Al-11 at % Cu is investigated by molecular dynamics (MD) simulations utilizing second nearest neighbor modified embedded atom method (2NN-MEAM) interatomic potential. The condition for directional solidification is produced by imposing dissimilar temperatures at the model boundaries along the [100] solidification direction to create a temperature gradient. During solidification, the solid-liquid front travels through the Al-Cu liquid along the [100] direction towards the high temperature end. At the initial stages of solidification, several solidification defects such as twins, stacking faults, and grain boundaries form. As directional solidification progresses, grains elongate along the solidification direction, and at the final stages of solidification no new defects or grain boundaries form. The elongated grain boundaries form a few layers with lamellar like structures along [100]. When the solidified polycrystalline is deformed in the [001] direction, glide of partial dislocations happen around the grain boundaries, whereas during elongation along [100] some defects from in the Al-Cu matrix. Since formation of defects requires more energy, the solidified samples show a higher tensile strength and strain when deformed along the [100] solidification direction.

Keywords: A1. Directional solidification; A1. Nucleation; A1. Defects; A1. Computer simulation; B1. Alloys.

[*]Corresponding author; email: zaeem@mines.edu (M. Asle Zaeem)

1. Introduction

Rapid directional solidification is an integrated part of several manufacturing processes both in conventional casting and modern processes like additive manufacturing [1-3]. Besides the overall importance of determining the processing-structure-property relations in manufacturing processes, study directional solidification can also provide important insights into the fundamentals of instabilities at the solid-liquid interfaces which result in complex nano/microstructures (e.g., dendrites).

Direct observation of nano/microstructural evolution during solidification of metals and alloys is difficult, and theoretically and numerically enriched mesoscale methods, such as phase-field [4-6], has been frequently applied to study dendritic structures in solidification, which require lower length scale information such as solid-liquid interface properties [7]. There are different computational methods that have been used to study solid-liquid coexistence properties, such as density functional theory (DFT) [8], MD [9, 10], Monte Carlo (MC) [11], front tracking (FT) model [12], and extended finite element method (FEM) [13, 14]. The main issues associated with most of these methods are their length scale and their accuracy. Solidification in metallic systems begins at the atomistic realm at the interior part of the liquid, and microscale computational methods, such as the phase-field method, cannot predict the nucleation stages. On the other hand, DFT studies can be used to investigate melting properties but they are limited to very small scales preventing them from directly observing solidification from atomistic scale. MC simulations are also performed in a much smaller scale, whereas FT or FEM methods for solidification are in trhe larger scale and less predictive. Among all these methods, MD has gained popularity in nucleation-solidification research due to its suitable length scale [15].

MD simulations have been used to study solidification from a few thousand atoms to multibillion atom systems [16, 17]. Along with having a flexible length scale in the range of a few nanometers to a few hundred nanometers, solidification studies by MD simulations could be very accurate depending on the interatomic potentials [18, 19]. In our previous works [10, 20] and some other recent MD studies [21-23], it was shown that a good agreement exists between MD predicted data and experimental and classical nucleation theory (CNT) results for critical nucleus size, nucleation temperature, incubation time and other solidification characteristics. However, MD simulations for study rapid directional solidification process is rare and is of great interest for

additive manufacturing community [24-27]. There was only one MD simulation study of directional growth which utilized the Lennard-Jones binary mixture model by Coura et al. [28], and to the best of our knowledge there is no MD simulation study of directional solidification for realistic metallic system by utilizing MD simulation, and also predicting the mechanical properties of spontaneously solidified structures is also very rare [20].

In the current study, we perform rapid directional solidification of Al-Cu alloy (Al 11 at% Cu) utilizing MD simulations by applying three different temperature gradients. 11 at% Cu is chosen as the case study because there will be sufficient Cu to increase the melting point of pure Al, and also the system will have sufficient Cu to produce some amount of Al_2Cu precipitation and segregation of Cu at grain boundaries (GBs). The directional solidification produces polycrystalline structures. Solidification features of the such as twin formation, GB formation, Cu segregation and precipitations are also studied. Finally, the solidified polycrystalline Al-Cu alloy is deformed by a uniaxial tensile load. The effect of strain rates and the loading direction are studied. To this extent, this study of directional-solidification can be considered as an initial step to bridge the gap between different length scales and also provide fundamental knowledge on processing-structure-property relations.

2. Computational Methodology

2.1. Interatomic Interactions

In Al-11 at% Cu mixture there are three fundamental interactions between atoms: Al-Al, Cu-Cu and Al-Cu. The second nearest neighbor modified embedded atom method (2NN MEAM) interatomic potential of Al developed by Lee and Baskes [29] was used is this work for the interaction between Al-Al and Cu-Cu. We recently tested this interatomic potential which showed reliable predictions of low and high temperature properties of Al and Cu [10, 18]. Table 1 shows the detailed properties of Al and Cu predicted by 2NN-MEAM MD simulations. The interatomic potential was recently extended for Al-Cu interactions, which also shows good agreement with experimental phase diagram of Al-Cu (up to 33 at% Cu) and various properties of Al2Cu θ/θ' [30].

Table 1. The low temperature elastic properties and high temperature melting properties of Al predicted by 2NN-MEAM MD simulations.

Properties	Al		Cu	
	Experiments	MEAM MD [18]	Experiments	MEAM MD [19]
Bulk Modulus (GPa)	76.4[a]	79.4	143.5[a]	166
C_{11} (GPa)	111.5[a]	114.3	176.8[a]	176.8
C_{12} (GPa)	58.8[a]	61.9	126.9[a]	125.0
C_{44} (GPa)	29.5[a]	31.6	81.8[a]	81.8
Specific Heat (J mol^{-1} K^{-1})	26.15[b]	24.70	25.30[b]	24.50
Thermal Expansion Coeff. (10^6 K^{-1})	17.31[b]	23.50	14.76[b]	17.0
Melting Point (T_m) (K)	934[c]	925	1357[c]	1320
solid–liquid interface free energy (mJ/m^2)	168.9±21 to 158±30[d]	172.6	237±26 to 270[d]	255.0

[a] Reference [31] , [b] Reference [32], [c] Reference [32-34], [d] Reference [35-37].

2.2. Simulation Details

The Al-Cu simulation box with size of $50\times50\times50$ nm^3 ($125\times125\times125$ unit cells, with ~8 M atoms) was created by randomly distributing 11 at% Cu in Al. Fig. 1(a) shows the initial dimensions for the simulation box. To prepare the homogenous Al-Cu melt, the simulation box of fcc crystalline Al-Cu was equilibrated at 1,500 K for 150 ps with a time step of 3 fs. The crystalline structure almost immediately becomes liquid, however to get a homogenous liquid structure it is equilibrated 150 ps. Temperature and pressure were controlled by Nose-Hoover thermostat and Parrinello-Rahman barostat [38], respectively. Periodic boundary conditions were employed in all three directions during the melt preparation. All the MD simulations were performed in parallel LAMMPS [39] code. The OVITO visualization package was used to monitor the melting, solidification and deformation processes [40]. Within OVITO, common neighbor analysis (CNA) was used [41] to identify the local crystalline structure of atoms. We also utilized orientation coloring to study the grain orientations. CNA was used to identify the primary fcc crystal structures. These fcc atoms are always align along the coordination axes (i.e., x', y', z'), but these

coordination axes are not always aligned with the principle axes (i.e., x, y, z) of simulation box. The orientation coloring shows, orientation of the grains from the principle axes, and for the coloring purposes we only considered the orientation from the principle axis Z. The coloring scheme was applied in OVITO, and the details of the implementation can be found in Larsen et al. work [42].
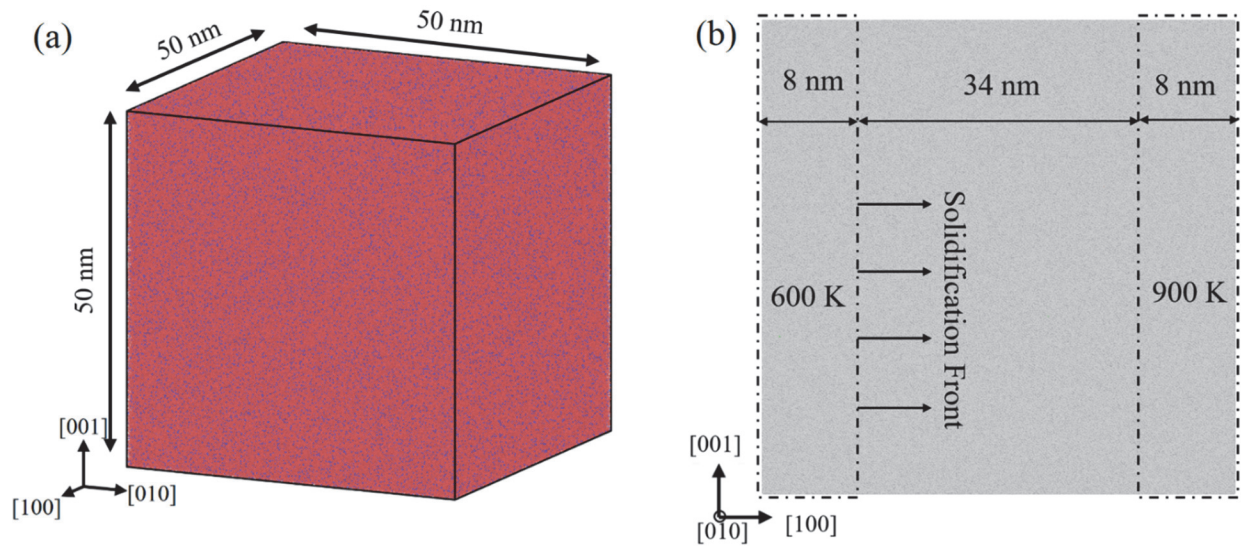

Fig. 1. Simulation box at (a) initial melt with temperature of 1,500 K. The red atoms are Al and 11 at% Cu is distributed in the Al matrix is colored blue. (b) The initial simulation set up for the directional solidification. The solid front travel in the [100] direction towards the hotter region (900 K in this case).

To facilitate directional solidification, two regions are created at the two end of the simulation box in the [100] direction, Fig. 1(b). The low temperature region is kept at a constant temperature of 600 K, and three different temperatures (800 K, 850 K and 900 K) is applied at the high temperature region for three distinct simulations. We refer to the 600-800 K box as Case-1, 600-850 K box as Case-2, and 600-900 K box as Case-3 throughout the paper. The melting point of Al and Cu are 933 K and 1358 K. As the phase diagram suggests, the melting point of Al with 11 at % Cu remains in the range of 850-900K [43]. The Al, Cu and Al-Cu should ideally solidify at ~600 K during the directional simulations. Moreover, once a part of the simulation box is solidified at 600 K, that will act as a seed for the rest of the simulation box. At the two temperature

regions, each with 8 nm thickness (Fig. 1(b)), the temperature is kept constant by applying Langevin thermostat. The temperature is not controlled for 34 nm region in the middle region creating a temperature gradient. Non-periodic boundary condition was applied in the direction of the solidification. The details of the different simulations performed is provided in Table 2.

To study the deformation and determine the mechanical properties of solidified polycrystalline samples, the final Al-Cu solidified configurations are subjected to uniaxial tension along different directions. The polycrystalline Al-Cu samples are deformed under uniaxial tension at 300 K at two different strain rate of 10^9 and $10^{10}\,\text{s}^{-1}$. The strain rates will be referred as SR1 (10^9 s^{-1}) and SR2 ($10^{10}\,\text{s}^{-1}$) throughout the manuscript. Each deformation is repeated twice, one in the direction of the solidification, [100], and another perpendicular to the solidification direction, [001]. A single crystal Al-Cu is also deformed under the similar conditions to compare the deformation behavior and mechanical properties with the directionally solidified polycrystalline Al-Cu samples.

Table 2. Simulation cases; three different temperature gradients for directional solidification, and two strain rates for uniaxial tensile deformation in two directions (total of 3 solidification simulations and 12 deformation simulations). A single crystal Al-Cu is also deformed at the same strain rates and temperatures (2 cases).

Temperature Regions	600-800 K (Case-1), 600-850 K (Case-2), and 600-900 K (Case-3)
Strain rate (s^{-1})	10^9 (SR1) and 10^{10} (SR2)
Deformation temperature	300 K

3. Results and Discussion
3.1. Directional Solidification

In rapid directional solidification process, serval twins form (red atoms in Fig. 2(a) and (b)) inside the fcc grains (green atoms in Fig. 2(a) and (b)), especially in the beginning of the process when smaller grains are forming. At each spontaneous time, the solidified part of the Al-Cu simulation box acts as solid seeds for rest of the liquid. The solidification font moves towards the liquid and gradually transform it into solid crystalline. The new solid formation happens in a much slower pace than the initial solidification, as a result there is not much defects or twins observed after initial solidification stages. Three dimensional (3D) views are shown in Fig. 2(b) and (c). The

grains generally elongate along the temperature gradient. Fig. 2(c) shows the grain boundaries (GBs) and grain orientations. Initially several randomly orientated grains form, however as the solidification font travelled towards the liquid region, many of them dissolved in the surviving grains. It can be also visualized from Fig. 2 that only few grains actually elongate.
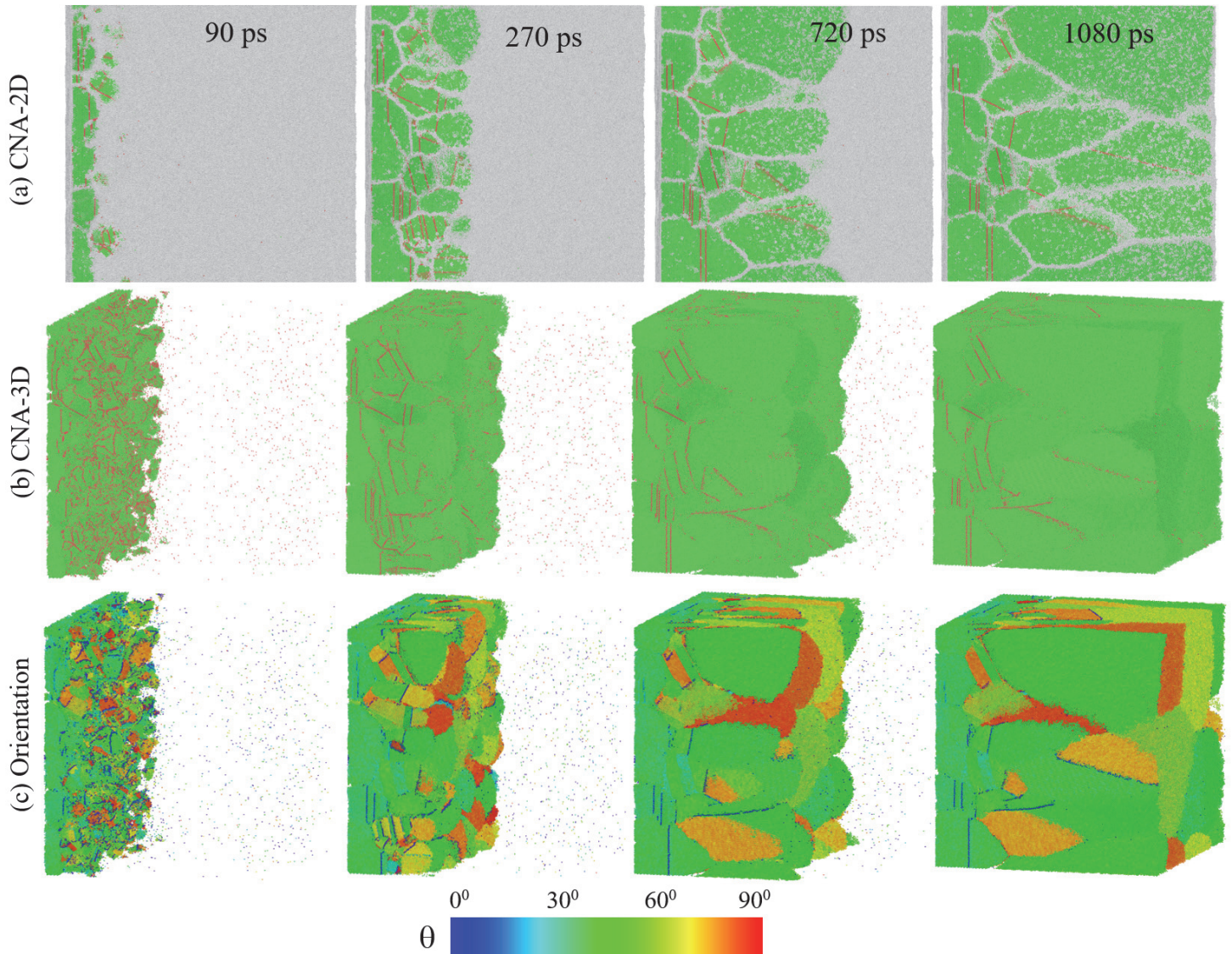

Fig. 2. Snapshots of the directional solidification of Al-11 at% Cu for Case-3 solidification. (a) 2D and (b) 3D views of solidification font travelling through the simulation box; atoms are colored by CNA coloring: green atoms are fcc, red atoms are hcp and the white atoms represents the liquid and amorphous solids. (c) 3D views of grains forming during the solidification with different orientations.

The average temperature was measured along the solidification direction and shown in Fig. 3(a). The temperature gradually increases from the lower to the higher temperature region. The amount of solidified Al-Cu can also be identified from the percentage of crystalline atoms, which is plotted in Fig. 3(b).
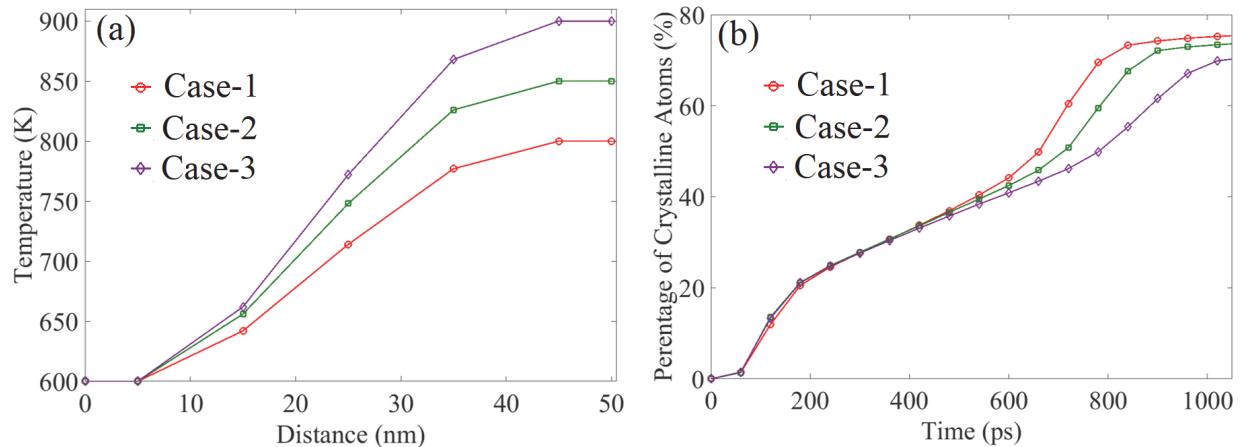

Fig. 3. (a) Average temperature of atoms along the [100] solidification direction for three different initial simulation set ups. (b) Number of crystalline atoms in each of the simulations during the solidification.

3.2. Formation of Twins and Detwinning

Directional solidification creates different types of nanostructures in different planes. The nanostructures in the (001) plane (Fig. 4(a) and (010) plane (Fig. 4(b)) look very similar; at the left side of the domain, where initial stage of solidification occurs, smaller grain sizes and both coherent twin boundaries (CTBs) and five-fold twin are present. Fig. 4(d) and (e) show 3D and 2D slices of planes from the simulation box along the (100) plane. Only CTBs are seen in the (100) plane. As the solidification progresses and some grains become elongated and larger, no CTBs or five-fold twins are observed. The average grain size in (010) plane is shown in a trapezoidal form in Fig. 5 for Case-2 solidification.

Fivefold twins are observed during the initial stages of solidification, as shown in Fig. 4(a) and (b). In general, fivefold twinning can happen in metals in a layer-by-layer growth during nucleation, successive growth twinning, or by deformation [44]. We previously observed formation of similar fivefold twins in solidification of pure Al [45], and the process of forming successive twin boundaries is similar to what we observe here for Al-11 at% Cu. During the initial

8

stages of solidification and packing of atoms to form nanocrystalline fcc Al, small size ordered subunits of hcp atoms also form as twin boundaries to compensate the angular misfit between different fcc growth planes. Formation of CTB and fivefold twins is consistent with the literature data on other fcc metals [44, 46, 47]. Also, fivefold twin structure formations by successive twinning growth on alternate cozonal twin planes was also previously observed in the solid phase crystallization of metal [48]. However, in our cases of directional solidification, formation of fivefold twins is only possible at the (001) and (010) planes. In the (100) plane, which is the solidification font, no multifold twins are observed (Fig. 4(e)). We can also observe from Fig. 4(e) that the grains from slice II to slice IV gradually become defect free.
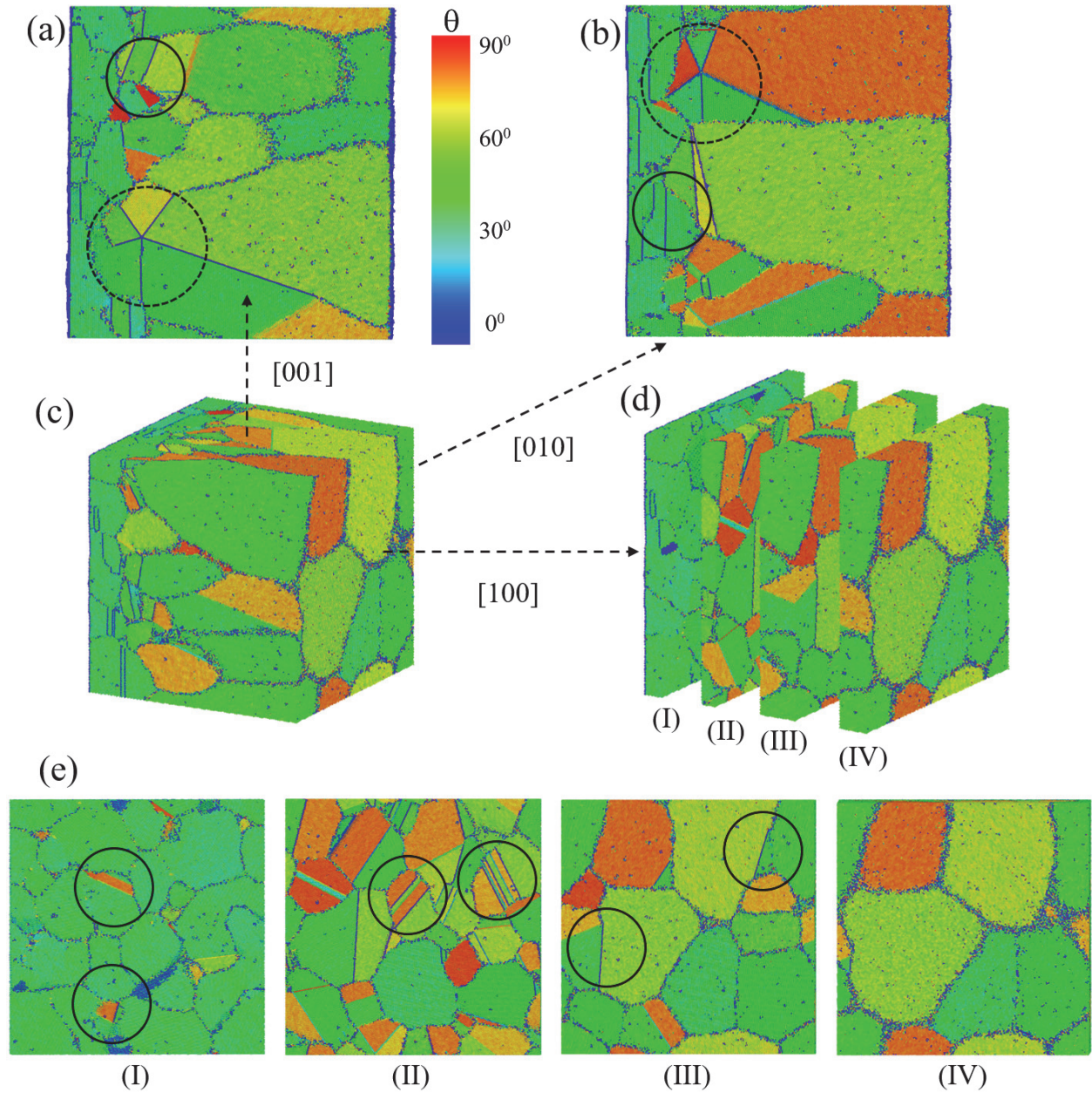
Fig. 4. Orientation coloring of the twins and nanostructures of the directional solidification for sample Case-3. (a) Twins and GBs are viewed from the top of the simulation box, (b) the grains and twins along the [100] solidification direction viewed from [010] direction, (c) the entire simulation box and the arrows shows the viewing directions (d) four layers has been sliced along the [100] solidification direction to observed the nanostructure facing the solidification font, (e) the nanostructures corresponding to the slices made in (d). The solid circles show coherent twin boundaries and dotted circles show fivefold twinning.
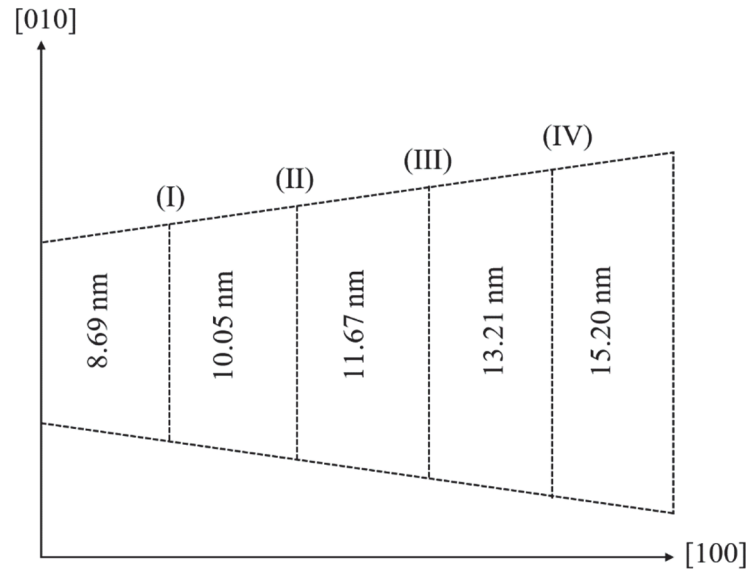
Fig. 5. The effective average grain size (or diameters) on the (010) plane along the solidification direction for Case-3.

3.3. Cu Segregation at Grain Boundaries

Previously, Cu segregation in Al-Cu alloys was studied by atom probe tomography in Al-5 at% Cu [49], and Al-2 at% Cu [50], and MD simulation was only used to study the solid-state segregation of Cu to GBs by strain effects [51]. Al and Cu both are fcc, however there is a lattice mismatch between Al and Cu: the lattice constant for Al is 4.05 Å and Cu is 3.59 Å. As mentioned by Liu et al. [51], there is a strain effect that mediates diffusion of Cu atoms to GBs. To investigate and visualize Cu segregation during solidification and possible formation of precipitates, a slice with 5 nm thickness from the simulation box is taken (dotted plane in Fig. 6(a)). First, we visualize the copper atoms on the solidification font, and the 3D surface mesh in Fig. 6(b) shows the topology of the solidification front; the blue Cu atoms are shown at the grain surfaces and GBs. This results suggests segregation of Cu atoms from the primary Al-Cu matrix onto GBs. Fig. 6(c) shows the [100] plane at the slice shown in Fig. 6(a); crystalline fcc and GBs contain both Al and Cu atoms. In Fig. 6(d), Al atoms are removed and only Cu atoms are shown. It is clear that a large number of Cu atoms are deposited or segregated at the GBs.

To measure the Cu segregation on the GB, we used the same slice of the simulation in Fig. 6(a). This surface is chosen from a distance of 10 nm from isothermal region at 600 K. In this way,

the chosen slice has a spontaneous temperature of between 650 and 700 K (Fig. 3(a)) for different solidification cases. All the Al atoms are removed from this and only copper atoms are kept, then we calculated the ratio of Cu atoms on GBs to the all Cu atoms in the slice. The result is shown in Fig. 6(e); the percentage of Cu atoms on GBs gradually increases as the annealing progresses in that area. These results suggest that a portion of Cu segregation onto GBs happens during solidification. The majority of Cu segregation onto GBs of a region (for example the dotted slice in Fig. 6(a)) happens after the region is solidified and the solidification front has moved away from that region, basically when the region is being annealed at solid state.
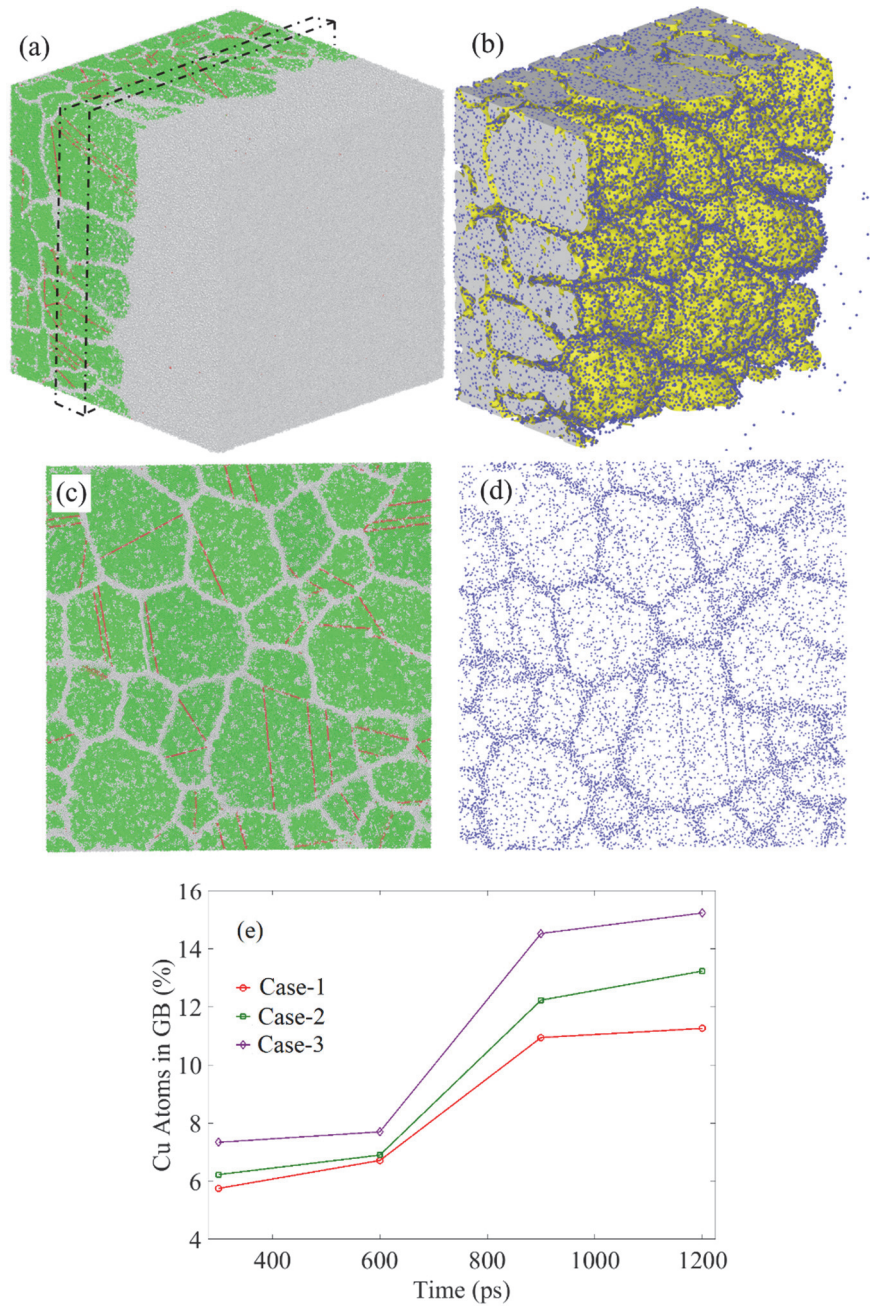
Fig. 6. (a) The 3-Dimesnional simulation box at 350 ps for Case-2. The dotted line shows the sliced planes for studying the interior of the solid font. (b) Surface mesh shows the copper atoms (blue) at the solid font and the GB regions. (c) The GB with both Al and Cu atoms from the sliced plane, (d) Only copper (blue) atoms shown on the GB and in the matrix.

3.4. Al$_2$Cu precipitation

If concentration of Cu atoms is locally increased, formation of Al_2Cu precipitates especially at the GBs is probable. In Fig. 7, two stages of solidification (450 ps and 900 ps) for the Case-1 solidification are presented. Both liquid and solid amorphous atoms are shown and then we performed coordination number (CN) analysis. The CN for Al_2Cu is derived to be remained within 12 to 13 for the temperature range between 600 to 800 K [52]. All Al and Cu atoms with crystalline fcc and hcp atoms are removed in Fig. 7. As Fig. 7 suggests, there are several precipitates that can be detected inside the grains and on the GBs. A low CN (blue or green colors) suggests that there is no particular structures for the liquid or solid atoms. The cluster of red atoms is having the exact CN for Al_2Cu, so those atom clusters can be identified as Al_2Cu precipitates. One of the areas with high CN is enlarged in Fig. 7(c) where the bigger atoms represents the Cu and smaller atoms represents the Al, clearly shows a higher density of Cu atoms locally. Experimentally Al_2Cu-θ precipitates can reach have sizes in a range of 25-50 nm [53, 54], which is beyond the scope of this study. The GB thickness in all the solidification cases varied between 0.5-1.25 nm. Recent studies by Wang et al. [55] shows that lattice constant of tetragonal theta phase is 1.2-1.3 nm experimentally and also distributed over different planes of symmetry. To form an ideal Al_2Cu-θ phase there must be few layers of stacking of Al and Cu atoms [56]. Due to the limitation of length scale of MD simulations, the Al_2Cu-θ precipitates similar to those experiments cannot be detected directly in this work. If the simulation size can be extended to a few billion atoms (submicron length scale) and the solidification rate can be slowed down which requires longer simulation times, one can expect to visualize Al_2Cu-θ precipitates similar to those observed by scanning electron microscopy.
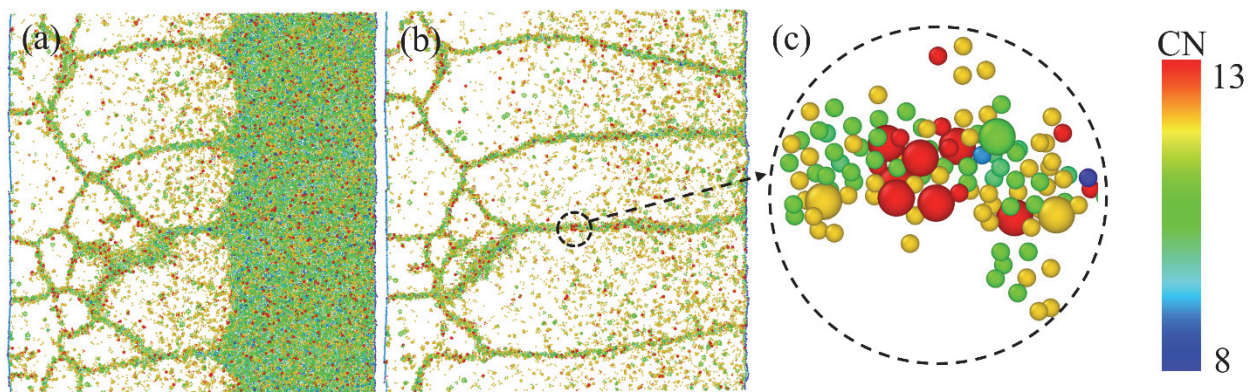

Fig. 7. (a) GBs facing the solid font in [100] direction for Case-1 solidification at 450 ps and (b) 900 ps. Atoms are colored with coordination number. All the crystalline fcc and hcp atoms are removed. Amorphous solid and liquid are having same coordination. (c) An enlarged GB area that

shows a much higher density of Cu and a high CN which is suitable for forming Al_2Cu precipitates. The bigger atoms represent Cu and smaller atoms represents Al.

3.5. Mechanical Properties after Directional Solidification

After obtaining the solidified polycrystalline structures of Al-11 at% Cu, the structures are deformed under uniaxial tension with two strain rates ($10^9 s^{-1}$ -SR1 and $10^{10} s^{-1}$ -SR2) along ([100]) and perpendicular ([001]) to the solidification direction. The typical deformation process is shown in Fig. 8. The snapshots on top of the stress-strain plot is the deformation along [100] direction and the bottom snapshots represents the deformation in the [001] direction. The trend for the stress strain curves are similar for all the other cases and strain rates in this work. The stress-strain curves in Fig. 8 indicate the ductile nature of the polycrystalline Al-Cu alloy. After the simulation box reaches the elastic limit and plastic begins, partial dislocations glide in the opposite direction of deformation for tensile stress along [100] direction. Consequently, detwinning happens with a combination of reduction in twin thickness and the layer-by-layer twin boundary removal by the opposite glide of partial dislocations with a Burgers vector ($\frac{1}{2}[10\bar{1}]$) identical to that of the twinning partial dislocations. Typical detwinning of deformation twins is also observed while the sample is plastically deformed, which is similar to the observations in experimental work [57]. The stages of detwinning of deformation twins is similar to those of the solidification twins, and the details are discussed in our recent work [20]. The fivefold twins also detwin as the tensile deformation continues. The driving force behind the detwinning comes from the variation in the excess energy of the system during the tensile deformation.

As shown in the Fig. 8, the bottom snapshots don't show any detwinning phenomena for deformation along the [001] direction. The difference in newly formed deformation twins in two different deformation directions are significant. As shown in Fig. 8, the twins formed during deformation along [100] direction are much smaller than those formed by deformation along [001] direction. In the fcc crystal structure, the dislocations glide by $\frac{1}{2}[10\bar{1}](full) \rightarrow \frac{1}{6}[11\bar{2}](partial) + \frac{1}{6}[2\bar{1}\bar{1}](partial)$. When stretching in the solidification direction, the dislocations get compressed and only remain partial for most cases causing formation

15

of shorter twins, whereas deformation in [001] direction the dislocation can be stretched to a longer length and the defects becomes persistent. This is also another reason that UTS is lower when deforming perpendicular to the solidification direction.
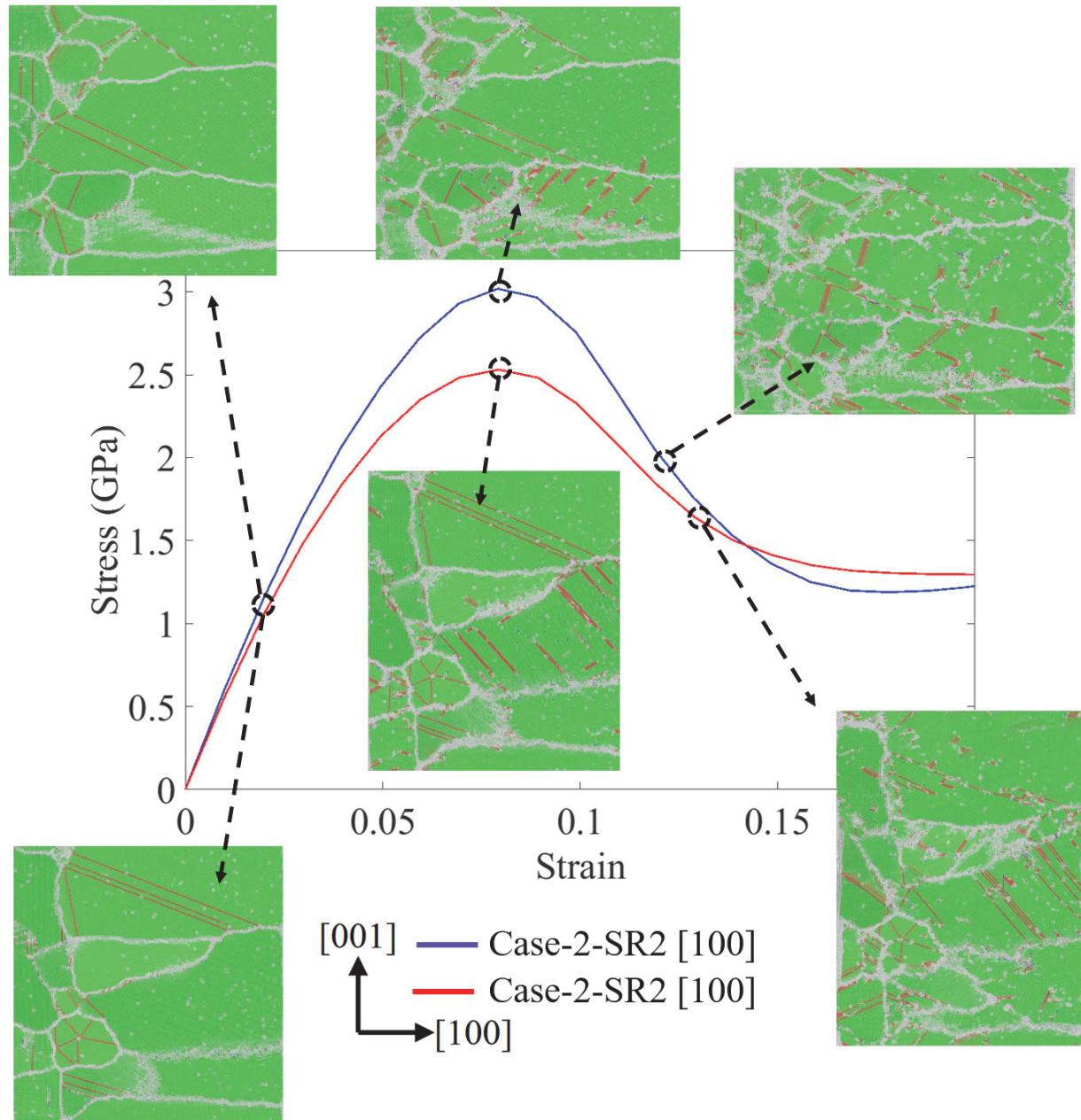

Fig. 8. Stress-strain curves for uniaxial deformation along and perpendicular to the solidification direction [001] of solidified Al-Cu for Case-2 at 300 K. The corresponding snapshot of the Al-Cu simulation box is also shown on the stress-strain plot. The [100] and [001] directions are same for all the deformation snapshots.

A detailed dislocation analysis is done in OVITO by utilizing DXA codes. The circuit length used is 1.4 nm and a stretchability of 9. Fig. 9(a) and Fig. 9(d) at $\varepsilon = 0.0$ shows CNA detection of initial dislocations inside the grains, which are shown in the dotted circles. The initial dislocation after solidification only shows the dislocations on the grain boundaries. As the tensile deformation is increased along the solidification direction and the alloy becomes plastic, the dislocations are stretched through the whole elongated grain, Fig. 9(c) and Fig. 9(f) at the strain of $\varepsilon = 0.12$. In some cases, these stretched dislocations form twin boundaries as well. As mentioned before, full dislocations form from the initial partial dislocation of $\frac{1}{6}[11\bar{2}]$. In Fig. 9(c) and (d), we show how a partial dislocation glide happens in the direction of the tensile deformation. Once the dislocations grow longer and form twin boundaries, the dislocations cannot be detected (Fig. 9(f)) as it either becomes a part of the fcc matrices or the hcp stacking faults/twins. Among the various different dislocations shown in Fig. 9(e), which is at $\varepsilon = 0.08$, only one remains in the form of a dislocation after the material is at $\varepsilon = 0.12$ (Fig. 9(f)). It can be noticed that the initial stacking faults of twins, which formed during the solidification process, also emit dislocations. The initial stacking faults shown in top part of Fig. 9(b), emit various dislocations once the simulation box is stretched further (Fig. 9(e)).

Fig. 9(g)-(l) show formation of partial dislocations in the $\frac{1}{6}[11\bar{2}]$ direction. We also detect some Hirth dislocations in the $\frac{1}{3}[00\bar{1}]$ direction along with Shockley partial dislocations where the dislocation emission occurs, Fig. 9(h) and Fig. 9(k). The most noticeable case here is the dislocation emission inside the grain due to the presence of initial twin boundaries. The key processes observed during the deformation of the solidified models include partial and full dislocation emission from the GBs and partial dislocation from inside the grains. The other influential factors in determining the deformation mechanism are CTB migration and interaction of the partial dislocations with fixed and migrating twin boundaries.
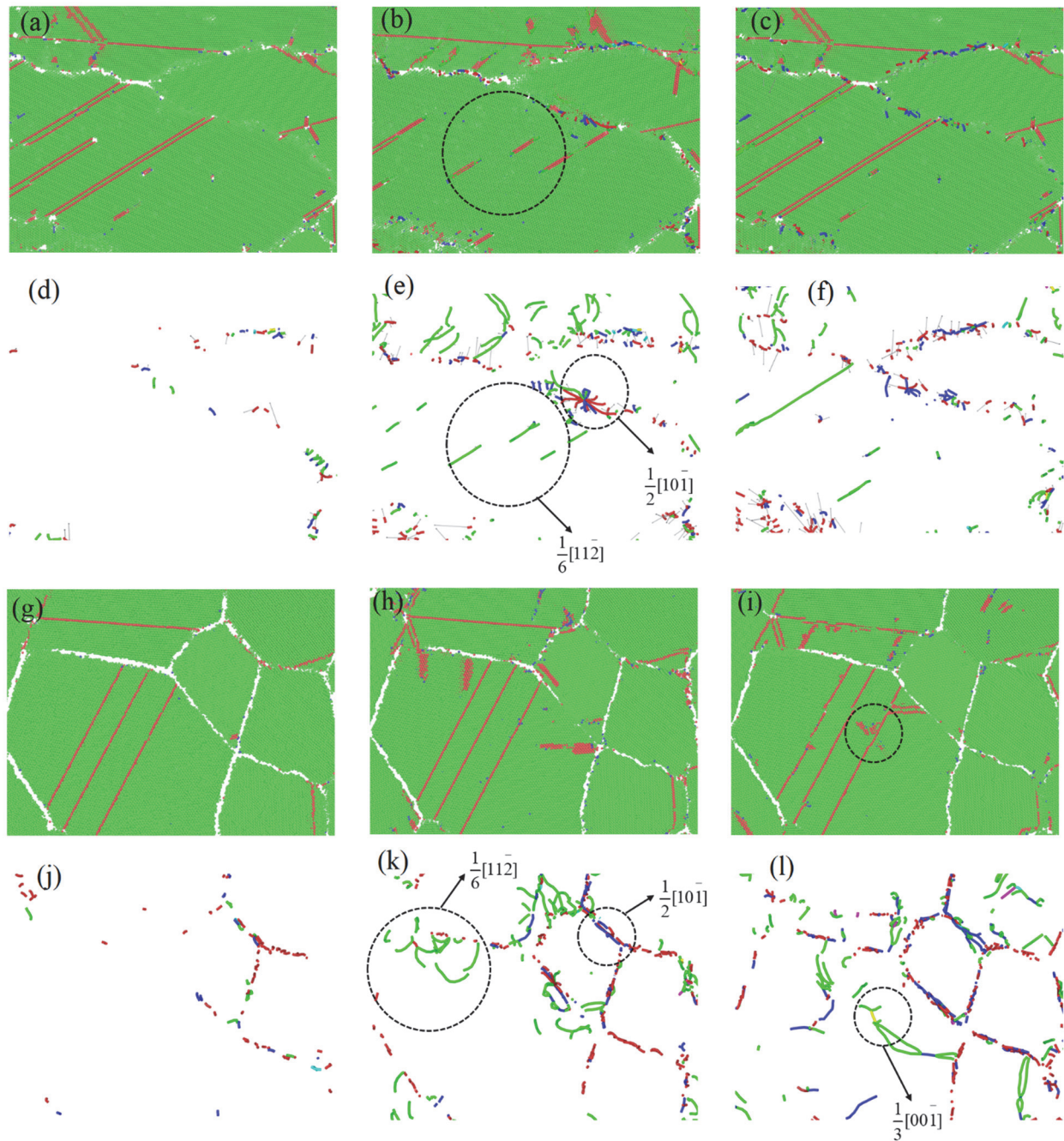
Fig. 9. Formation of dislocations and stacking faults during uniaxial deformation at 300 K (a-f) along, and (g-l) perpendicular to the solidification direction. The solidified Al-Cu structures for Case-2 was used for the deformation simulations. (a), (d), (g) and (j) are at strain of $\varepsilon = 0.0$, (b), (e), (h) and (k) are at strain of $\varepsilon = 0.08$, (c), (f), (i) and (l) are at strain of $\varepsilon = 0.12$. The corresponding snapshot is a slice of the Al-Cu simulation box on the [100] plane. The GBs were removed for detecting the dislocation inside the grains. (a), (b), (c), (g), (h) and (i) show CNA coloring, and (d), (e), (f), (j), (k) and (l) show the dislocations segments without the particles.

Stress-strain curves for different polycrystalline cases produced by rapid solidification are presented in Fig. 10 and compared with single crystal cases. Single crystal Al-Cu cases show a much higher yield stress, but fail immediately after the yield point us reached, suggesting a brittle behavior. The polycrystalline Al-Cu shows a long plastic region in the stress-strain plot. This indicates the ductile nature of polycrystalline Al-Cu and its ability to deform plastically. The stress–strain curve of polycrystalline Al-Cu under tensile loading has a trend identical to that of conventional polycrystalline metals, and it can be characterized into three stages: an initial elastic region, a yielding region, and a failure region. The ultimate tensile strength for single crystal Al-Cu is found to be 6.87 and 7.09 GPa for the strain rates of SR1 and SR2, respectively, which is much higher than the directionally solidified polycrystalline Al-Cu.

The failure strength for Al-11at% Cu remains in the range between 2 to 3 GPa for all the cases at different strain rates. The investigation of mechanical properties shows that the ultimate tensile strength (UTS) when deformed in the direction of solidification [100] is always higher than cases deformed perpendicular to the solidification direction, Fig. 9(b). Fig. 9(c) shows that the strain at UTS is also higher for cases deformed along [100] direction. This can be explained based on the grain orientations and the evolution of grains and twins during deformation. As shown in Fig. 2 and Fig. 4, during directional solidification grains forms in a lamellar pattern along [100] direction. Due to the formation of the elongated grains along [100] and lack of GBs oriented perpendicular to the solidification direction, the tensile deformation along [100] direction sees less influence from GBs. During the tensile deformation along the [001] direction, GBs act as weak links and somewhat cause discontinuity in the Al-Cu matrix, therefore a lower yield point and plasticity at a lower stress are expected.

The orientation and alignment of the twins inside the grains also play a crucial role on determining the UTS. As shown in Fig. 8 for the deformation along the solidification direction, partial dislocations glide in the opposite direction of twin boundary growth and also the [100] direction. Due to this reason the ultimate tensile strength as well as the ultimate tensile strain (Fig. 9(a-b)) both remain higher for deformation along the solidification direction. When deformed in the [001] direction the twins only get stretched, and once it becomes plastic there are several partial dislocation glides at the GBs.
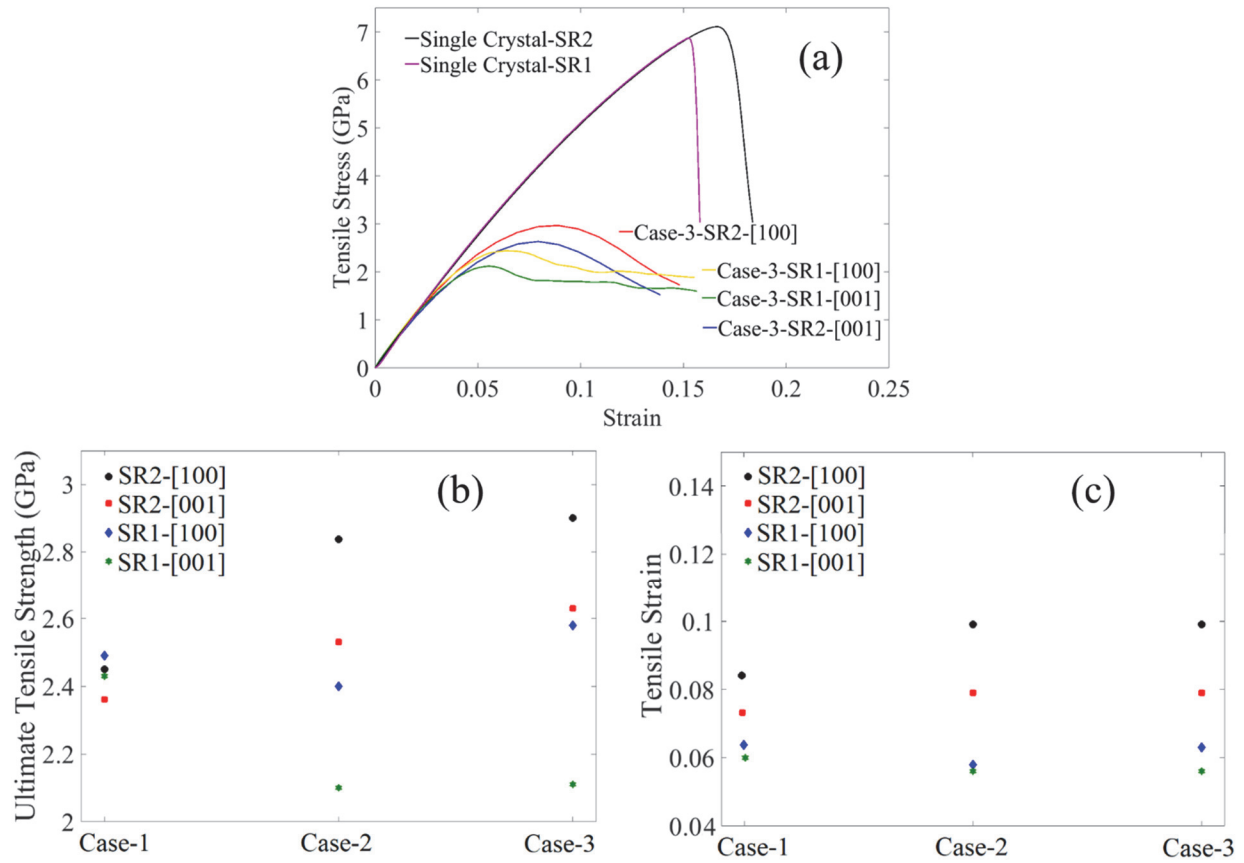
Fig. 10. (a) The comparison of strength of Al-Cu single crystal and directionally solidified polycrystalline Al-11 at% Cu. (b) The ultimate tensile strength and (c) tensile strain is shows for strain rate of 10^9 (SR1) and 10^{10} s^{-1} (SR2) along the solidification direction, [100], and perpendicular to the solidification direction, [001]. The different solidification model is shown in the X axis. All deformation is performed at 300 K.

4. Conclusion

In this paper, we performed MD simulations utilizing 2NN MEAM interatomic potential to study rapid directional solidification of Al-11 at% Cu, and studied Cu segregation, Al$_2$Cu precipitation and deformation mechanisms of solidified polycrystalline under uniaxial tension. Initial solidification was performed with three different temperature gradients, and then mechanical properties were studied by uniaxial tensile deformation under two different strain rates.

At the initial stages of solidification, several small grains, twin boundaries and GBs formed, but as solidification progressed only a few of these grains grew and elongated towards the solidification direction. These elongated grains contained less defects, twins or GBs. The elongation of GBs also formed a layer by layer fcc matrix along the solidification direction. As the solidification font traveled along the [100] direction, some Cu atoms segregated to the liquid side of the solid-liquid interface, and the Cu segregation increased gradually during annealing after the region was solidified. The percentage of segregated Cu atoms increased as the solidification proceeds. Utilizing CN analysis, Al_2Cu precipitations were identified in the solid and liquid and at the GBs.

Deformation simulations suggested that the directionally solidified Al-Cu alloy has more strength when deformed in the direction of the solidification than other directions. When the simulation box was deformed perpendicular to the solidification direction, deformation occurred easier because GBs which are weak links were perpendicular to the loading direction. Also, the newly formed deformation twins by partial dislocation glide, aligned along $\frac{1}{2}[10\bar{1}]$ direction, got stretched in the [001] direction and caused the Al-Cu matrix to fail at a lower strength than [100] direction.

Overall, we demonstrated some capabilities of MD simulations in study of rapid directional solidification of a binary system. With larger computational resources, solidification studies of metallic alloys in submicron scale are possible and comparable to experimental data. In the future, this computational approach can be applied to more realistically replicate several fundamental aspects of manufacturing processes involving solidification.

Acknowledgments

References

[1] M. Gündüz, E. Çadırlı, Directional solidification of aluminium–copper alloys, Materials Science and Engineering: A 327(2) (2002) 167-185.

[2] M. Gäumann, R. Trivedi, W. Kurz, Nucleation ahead of the advancing interface in directional solidification, Materials Science and Engineering: A 226 (1997) 763-769.

[3] I. Gibson, D.W. Rosen, B. Stucker, Additive manufacturing technologies, Springer2014.

[4] W.J. Boettinger, J.A. Warren, C. Beckermann, A. Karma, Phase-field simulation of solidification, Annual review of materials research 32(1) (2002) 163-194.

[5] A. Karma, Phase-field formulation for quantitative modeling of alloy solidification, Physical Review Letters 87(11) (2001) 115701.

[6] M. Asle Zaeem, H. Yin, S.D. Felicelli, Modeling dendritic solidification of Al–3%Cu using cellular automaton and phase-field methods, Applied Mathematical Modelling 37(5) (2013) 3495-3503.

[7] S. Kavousi, B.R. Novak, M. Asle Zaeem, D. Moldovan, Combined molecular dynamics and phase field simulation investigations of crystal-melt interfacial properties and dendritic solidification of highly undercooled titanium, Computational Materials Science 163 (2019) 218-229.

[8] Y.A. Chang, S. Chen, F. Zhang, X. Yan, F. Xie, R. Schmid-Fetzer, W.A. Oates, Phase diagram calculation: past, present and future, Progress in Materials Science 49(3-4) (2004) 313-345.

[9] M.H. Grabow, G.H. Gilmer, A.F. Bakker, Molecular dynamics studies of silicon solidification and melting, MRS Online Proceedings Library Archive 141 (1988).

[10] A. Mahata, M. Asle Zaeem, M.I. Baskes, Understanding homogeneous nucleation in solidification of aluminum by molecular dynamics simulations, Modelling and Simulation in Materials Science and Engineering 26(2) (2018) 025007.

[11] A. Das, S. Ji, Z. Fan, Morphological development of solidification structures under forced fluid flow: a Monte-Carlo simulation, Acta Materialia 50(18) (2002) 4571-4585.

[12] M. Zhu, C. Hong, D. Stefanescu, Y. Chang, Computational modeling of microstructure evolution in solidification of aluminum alloys, Metallurgical and Materials Transactions B 38(4) (2007) 517-524.

[13] J. Chessa, P. Smolinski, T. Belytschko, The extended finite element method (XFEM) for solidification problems, International Journal for Numerical Methods in Engineering 53(8) (2002) 1959-1977.

[14] A. Dalhuijsen, A. Segal, Comparison of finite element techniques for solidification problems, International journal for numerical methods in engineering 23(10) (1986) 1807-1829.

[15] D.C. Rapaport, D.C.R. Rapaport, The art of molecular dynamics simulation, Cambridge university press2004.

[16] K. Kadau, T.C. Germann, P.S. Lomdahl, Molecular dynamics comes of age: 320 billion atom simulation on BlueGene/L, International Journal of Modern Physics C 17(12) (2006) 1755-1761.

[17] Y. Shibuta, S. Sakane, E. Miyoshi, S. Okita, T. Takaki, M. Ohno, Heterogeneity in homogeneous nucleation from billion-atom molecular dynamics simulation of solidification of pure metal, Nature Communications 8(1) (2017) 10.

[18] E. Asadi, M. Asle Zaeem, S. Nouranian, M.I. Baskes, Two-phase solid–liquid coexistence of Ni, Cu, and Al by molecular dynamics simulations using the modified embedded-atom method, Acta Materialia 86 (2015) 169-181.

[19] E. Asadi, M. Asle Zaeem, S. Nouranian, M.I. Baskes, Quantitative modeling of the equilibration of two-phase solid-liquid Fe by atomistic simulations on diffusive time scales, Physical Review B 91(2) (2015) 024105.

[20] A. Mahata, M. Asle Zaeem, Evolution of solidification defects in deformation of nano-polycrystalline aluminum, Computational Materials Science 163 (2019) 176-185.

[21] M. Horsch, J. Vrabec, H. Hasse, Modification of the classical nucleation theory based on molecular simulation data for surface tension, critical nucleus size, and nucleation rate, Physical Review E 78(1) (2008) 011603.

[22] X.-M. Bai, M. Li, Test of classical nucleation theory via molecular-dynamics simulation, The Journal of chemical physics 122(22) (2005) 224510.

[23] G.C. Sosso, J. Chen, S.J. Cox, M. Fitzner, P. Pedevilla, A. Zen, A. Michaelides, Crystal nucleation in liquids: Open questions and future challenges in molecular dynamics simulations, Chemical reviews 116(12) (2016) 7078-7116.

[24] E. Herbold, O. Walton, M. Homel, Simulation of powder layer deposition in additive manufacturing processes using the discrete element method, Lawrence Livermore National Lab.(LLNL), Livermore, CA (United States), 2015.

[25] Z. Hu, S. Mahadevan, Uncertainty quantification and management in additive manufacturing: current status, needs, and opportunities, The International Journal of Advanced Manufacturing Technology 93(5-8) (2017) 2855-2874.

[26] A. Sorkin, J. Tan, C. Wong, Multi-material modelling for selective laser melting, Procedia engineering 216 (2017) 51-57.

[27] T.Q. Vo, B.H. Kim, Molecular dynamics study of thermodynamic properties of nanoclusters for additive manufacturing, International Journal of Precision Engineering and Manufacturing-Green Technology 4(3) (2017) 301-306.

[28] P.Z. Coura, O.N. Mesquita, B.V. Costa, Molecular-dynamics simulation of directional growth of binary mixtures, Physical Review B 59(5) (1999) 3408-3413.

[29] B.-J. Lee, M. Baskes, Second nearest-neighbor modified embedded-atom-method potential, Physical Review B 62(13) (2000) 8564.

[30] A. Mahata, M. Asle Zaeem, Modified embedded atom method potential for binary Al alloys for melting and solid-liquid coexistence properties, Submitted to Acta Materillia (2019).

[31] G. Simmons, H. Wang, Single crystal elastic constants and calculated aggregate properties, (1971).

[32] W.F. Gale, T.C. Totemeier, Smithells metals reference book, Butterworth-Heinemann2003.

[33] A.M. James, M.P. Lord, Macmillan's chemical and physical data, Macmillan1992.

[34] J.G. Speight, Lange's handbook of chemistry, McGraw-Hill New York2005.

[35] Q. Jiang, H. Lu, Size dependent interface energy and its applications, Surface Science Reports 63(10) (2008) 427-464.

[36] L. Gránásy, M. Tegze, A. Ludwig, Solid–liquid interfacial free energy, Rapidly Quenched Materials, Elsevier1991, pp. 577-580.

[37] M. Gündüz, J. Hunt, The measurement of solid-liquid surface energies in the Al-Cu, Al-Si and Pb-Sn systems, Acta Metallurgica 33(9) (1985) 1651-1672.

[38] M. Parrinello, A. Rahman, Polymorphic transitions in single crystals: A new molecular dynamics method, Journal of Applied physics 52(12) (1981) 7182-7190.

[39] S. Plimpton, Fast parallel algorithms for short-range molecular dynamics, Journal of computational physics 117(1) (1995) 1-19.

[40] A. Stukowski, Visualization and analysis of atomistic simulation data with OVITO–the Open Visualization Tool, Modelling and Simulation in Materials Science and Engineering 18(1) (2009) 015012.

[41] H. Tsuzuki, P.S. Branicio, J.P. Rino, Structural characterization of deformed crystals by analysis of common atomic neighborhood, Computer physics communications 177(6) (2007) 518-523.

[42] P.M. Larsen, S. Schmidt, J. Schiøtz, Robust structural identification via polyhedral template matching, Modelling and Simulation in Materials Science and Engineering 24(5) (2016) 055007.

[43] V.S. Zolotorevsky, N.A. Belov, M.V. Glazoff, Casting aluminum alloys, Elsevier Amsterdam2007.

[44] H. Hofmeister, Forty Years Study of Fivefold Twinned Structures in Small Particles and Thin Films, Crystal Research and Technology 33(1) (1998) 3-25.

[45] T. Shen, Y. Wu, X. Lu, Structural evolution of five-fold twins during the solidification of Fe 5601 nanoparticle: a molecular dynamics simulation, Journal of molecular modeling 19(2) (2013) 751-755.

[46] A.J. Cao, Y.G. Wei, Formation of fivefold deformation twins in nanocrystalline face-centered-cubic copper based on molecular dynamics simulations, Applied Physics Letters 89(4) (2006) 041919.

[47] Y.T. Zhu, X.Z. Liao, R.Z. Valiev, Formation mechanism of fivefold deformation twins in nanocrystalline face-centered-cubic metals, Applied Physics Letters 86(10) (2005) 103112.

[48] J. Narayan, Dislocations, twins, and grain boundaries in CVD diamond thin films: Atomic structure and properties, Journal of Materials Research 5(11) (1990) 2414-2423.

[49] C. Srivastava, G. Thompson, D. Reinhard, J. Sebastian, T. Prosa, D. Larson, Z. Reddy, S. Gupta, W. Butler, M. Weaver, Atom Probe Tomography of Al-Cu Precipitation in an Al-5 at.%Cu Thin Film, Microscopy and Microanalysis 12(S02) (2006) 1752-1753.

[50] P.-P. Choi, T. Al-Kassab, R. Kirchheim, Investigation of sputter-deposited Al–2at.%Cu layers by means of the tomographic atom probe (TAP), Scripta Materialia 53(3) (2005) 323-327.

[51] X.-Y. Liu, W. Xu, S.a. Foiles, J. Adams, Atomistic studies of segregation and diffusion in Al-Cu grain boundaries, Applied physics letters 72(13) (1998) 1578-1580.

[52] L. Xiong, F. Guo, X. Wang, Q. Cao, D. Zhang, Y. Ren, J. Jiang, Structural evolution and dynamical properties of Al2Ag and Al2Cu liquids studied by experiments and ab initio molecular dynamics simulations, Journal of Non-Crystalline Solids 459 (2017) 160-168.

[53] G. Simmons, Single crystal elastic constants and calculated aggregate properties, SOUTHERN METHODIST UNIV DALLAS TEX, 1965.

[54] Y. Huang, J.D. Robson, P.B. Prangnell, The formation of nanograin structures and accelerated room-temperature theta precipitation in a severely deformed Al–4wt.% Cu alloy, Acta Materialia 58(5) (2010) 1643-1657.

[55] L. Wang, W. Lu, Q. Hu, M. Xia, Y. Wang, J.-g. Li, Interfacial tuning for the nucleation of liquid AlCu alloy, Acta Materialia 139 (2017) 75-85.

[56] B. Yang, Y. Zhou, D. Chen, X. Ma, Local decomposition induced by dislocation motions inside precipitates in an Al-alloy, Scientific reports 3 (2013) 1039.

[57] B. Li, M. Sui, B. Li, E. Ma, S. Mao, Reversible twinning in pure aluminum, Physical review letters 102(20) (2009) 205504.